Assessment of DVC measurement uncertainty on GFRPs with various fiber architectures

Ante Bartulović[1], Zvonimir Tomičević[*2], Ante Bubalo[3] and François Hild[4]

[1]*INETEC - Institute for Nuclear Technology, Dolenica 28, 10250 Lučko, Croatia*
[2]*Faculty of Mechanical Engineering and Naval Architecture, University of Zagreb,*
Ivana Lučića 5, 10002 Zagreb, Croatia
[3]*Yazaki Europe Limited, Slavonska Avenija 26/6, 10000 Zagreb, Croatia*
[4]*Université Paris-Saclay, CentraleSupélec, ENS Paris-Saclay, CNRS, LMPS - Laboratoire de Mécanique*
Paris-Saclay, 91190 Gif-sur-Yvette, France

Abstract. The comprehensive understanding of the fiber reinforced polymer behavior requires the use of advanced non-destructive testing methods due to its heterogeneous microstructure and anisotropic mechanical proprieties. In addition, the material response under load is strongly associated with manufacturing defects (e.g., voids, inclusions, fiber misalignment, debonds, improper cure and delamination). Such imperfections and microstructures induce various damage mechanisms arising at different scales before macrocracks are formed. The origin of damage phenomena can only be fully understood with the access to underlying microstructural features. This makes X-ray Computed Tomography an appropriate imaging tool to capture changes in the bulk of fibrous materials. Moreover, Digital Volume Correlation (DVC) can be used to measure kinematic fields induced by various loading histories. The correlation technique relies on image contrast induced by microstructures. Fibrous composites can be reinforced by different fiber architectures that may lead to poor natural contrast. Hence, a priori analyses need to be performed to assess the corresponding DVC measurement uncertainties. This study aimed to evaluate measurement resolutions of global and regularized DVC for glass fiber reinforced polymers with different fiber architectures. The measurement uncertainties were evaluated with respect to element size and regularization lengths. Even though FE-based DVC could not reach the recommended displacement uncertainty with low spatial resolution, regularized DVC enabled for the use of fine meshes when applying appropriate regularization.

Keywords: digital volume correlation; fiber reinforced polymers; measurement uncertainty; mechanical regularization; X-ray computed tomography

1. Introduction

The characterization of Fiber Reinforced Polymers (FRPs) includes the assessment of defects due to manufacturing processes (Ray *et al.* 2007) as well as the detection and evaluation of the structural integrity of engineering components subjected to in-service conditions. Due to heterogeneous and anisotropic features of FRPs, it is particularly challenging to identify defects and damage since they may occur, as a result of applied loadings, at different locations and on various

---

∗Corresponding author, Assistant Professor, E-mail: zvonimir.tomicevic@fsb.hr

scales. Hence, it is necessary to apply robust and reliable Non-Destructive Testing (NDT) techniques to detect damage initiation and monitor the structural health (Wang *et al.* 2020). The choice of NDT techniques depends on the underlying microstructure, thickness of composites, signal attenuation and scattering, surface condition, accessibility for inspection, and the sought scale level. Wang *et al.* (2020) reported from the Web of Science Core Collection database that in the last two decades increased applications of X-ray Computed Tomography - XCT (Garcea *et al.* 2018, Rashidi *et al.* 2020) and Digital Image Correlation - DIC (Périé *et al.* 2002, Tekieli *et al.* 2017) were noted for NDT purposes.

XCT is nowadays a comprehensive and non-destructive technique for material inspection since the 3D microstructure is revealed. In the field of FRPs, their multiscale heterogeneity requires insight into the bulk of observed specimens. X-ray imaging provides information on manufacturing defects (Chambers *et al.* 2006, Mahadik *et al.* 2010) and on damage initiation and growth with respect to underlying microstructures (Arif *et al.* 2014, Scott *et al.* 2011, Arif *et al.* 2014, Garcea *et al.* 2015, Rolland *et al.* 2016).

Full-field measurement techniques are a complementary tool to measure the kinematics in loaded materials. DIC (Chu *et al.* 1985, Besnard *et al.* 2006) is one of the most used image processing methods in experimental mechanics. The measurand, namely, displacement fields are subsequently used to calculate strain maps that reveal localized phenomena arising in the material (Brynk *et al.* 2012), surface and bulk damage (Vrgoč *et al.* 2021a, b), and damage quantification (Hild *et al.* 2015). Furthermore, inverse identification procedures that employ displacement/strain fields measured with DIC to calibrate material parameters are well established (Lecompte *et al.* 2007, Gras *et al.* 2015).

High resolution 3D images of microstructures can be used for ex- or in-situ monitoring of damage growth as a function of loading conditions. The natural way to couple planar kinematic measurements and X-ray imaging was performed by extending the DIC methodology to 3D images (Bay *et al.* 1999, Roux *et al.* 2008). Kinematic fields in the bulk of composite materials are measured via Digital Volume Correlation (DVC) (Buljac *et al.* 2018a).

Nowadays, DVC is becoming a tool of choice to quantify various deformation (Lee *et al.* 2020) and failure mechanisms (Agyei *et al.* 2020). Furthermore, experimentally measured displacement fields are being used to drive 3D simulations for validation and identification purposes (Buljac *et al.* 2018b). The first challenge when dealing with 3D images is that actual microstructures can seldom be modified in the bulk to enhance contrast. Even though microstructural fiducial patterns may be created in the bulk of FRPs by adding various particles in the resin (Schöberl *et al.* 2020), such process may induce unwanted micromechanical phenomena. Second, the characterization of materials may be limited by side effects (i.e., artifacts) that arise in the (tomographic) reconstruction procedures. These imperfections have numerous sources (Davis and Elliott 2006) and are recognized as gray level variations or specific curves. Finally, acquisition noise, reconstruction artifacts, and the correlation procedure itself cannot find perfect match between the reference and deformed images. Hence, it is necessary to conduct systematic uncertainty quantifications (Buljac *et al.* 2018c, Croom *et al.* 2021).

The present investigation aims to evaluate DVC uncertainties on FRPs with four different fiber architectures. FE-based DVC (Roux *et al.* 2008) will be employed to measure displacements fields with different meshes in order to determine the minimal (i.e., necessary) discretization of volumetric images that can be applied on a certain fiber architecture. Further, FE-based DVC can be further regularized (Mendoza *et al.* 2019). The minimal regularization length that needs to be applied will be then determined to surpass the spatial resolution limit.
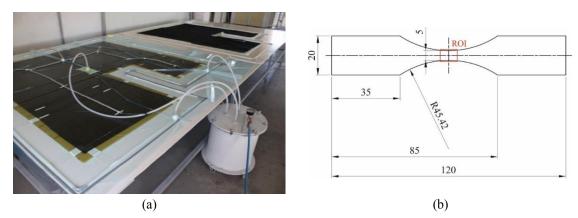
Fig. 1 (a) Vacuum infusion process of the four glass FRP plates with different fiber architectures. (b) Draft of the dogbone samples. The red contour depicts the scanned ROI

2. Material and acquisition protocol

2.1 Glass fiber reinforced composite and specimens

In this work, the measurement uncertainties were evaluated for vinylester resin reinforced with four different glass fiber architectures, namely, mat (MAT), cross-directional (CD), unidirectional (UD) and woven fabric (WF) layers. Four 5 mm in thickness FRP plates were produced in a single vacuum infusion process (Fig. 1(a)). This procedure was applied to prepare composite plates with dimensions of $1000\times1000\times5$ mm. In the proposed study, four dog-bone samples with different fiber architectures were machined with waterjet cutting.

The central part of the specimens was thinned since they were to be used for determining the tensile properties of such Glass Fiber Reinforced Polymers (GFRPs). Furthermore, it helped to initiate damage in the central part of the samples, which was monitored for DVC purposes. The samples were machined with a radius equal to 45 mm, and a ligament width of 5 mm (Fig. 1(b)), corresponding to plate thickness. The ligament cross-section specimen had a square shape (i.e., 5×5 mm) in order to the have approximately the same angular thickness for the scanned region of interest (ROI).

2.2 XCT scanning

The performance of DVC algorithms strongly depends on the ability to register microstructural features within the ROI. In the proposed case study, the contrast (i.e., image gradient) was achieved between the different constituents, namely, matrix, fibers and processing defects. In the absorption mode of X-ray CT, the contrast of the observed microstructure arises from different linear attenuation coefficients of the constituents.

The proposed investigation was conducted on a laboratory CT scanner, whose main elements were an X-ray source (i.e., tube), a turn table and an X-ray sensitive detector (Fig. 2). Different configurations of these components can be used to create CT scanners optimized for imaging objects of various sizes and compositions. The tube characteristics are the target material and peak X-ray energy, which determine the X-ray spectrum that is generated; the current, which

determines X-ray intensity; and the focal spot size, which impacts the spatial resolution. Conical X-ray beams are emitted from the source. When X-rays pass through an object, the intensity of the X-ray beam is reduced exponentially due to changes in the number, energy and direction of incoming photons. This complex intensity reduction mechanism is called attenuation. On the way through the dogbone specimen, part of the impinging radiation is absorbed. In order to use tomography on an object, several hundreds of two-dimensional radiographic images are acquired in sequences, with the object in various angular positions. The object is generally located on a turntable, which is gradually rotated step by step. In the proposed acquisition protocol, the specimen was mounted on a rig, which was aligned with the rotation axis of the pedestal that changed the angular position step-wise. The three-dimensional information about the object, which is contained in the series of radiographs, was reconstructed using a suitable algorithm to obtain voxel images.

Two consecutive scans for each investigated GFRP were acquired in the unloaded state (i.e., the sample was just mounted on the turntable, see Fig. 2). The acquisitions were conducted in a laboratory tomograph Werth TomoScope S, Yazaki Europe Limited, with the hardware parameters described in Table 1. The selected parameters (i.e., number of the projections and frame average) led to a total duration for a single scan of about two and a half hours. Such parameters reduced the noise level on the acquired projections. The definition of one radiograph was 1133×1461 pixels with a 2×2 binning. Even though image binning reduced the spatial resolution, it also decreased the noise level. The 3D image was reconstructed with a filtered back projection algorithm. The physical voxel length was 8.7 μm, and the reconstructed volume was encoded with 8-bit deep gray levels.

Qualitative information about composite architecture, fiber misalignment, processing defects of the investigated GFRP composites are shown in Fig. 3. The initial scan (of definition: 1133×1133×1461 voxels) was cropped to a volume size of 540×702×998 voxels. The extracted volume with an 8.7 μm/voxel resolution covered ca. 5.1×6×9 mm^3. From the reported mid-slices,
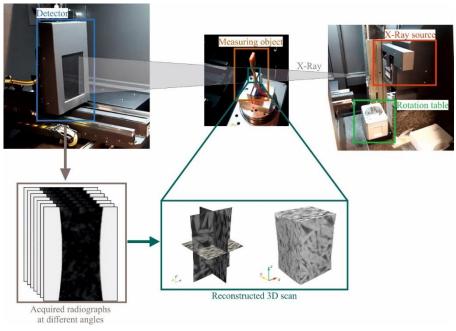

Fig. 2 Experimental setup shown for dogbone samples made of FRPs

Table 1 DVC hardware parameter

Tomograph	Werth TomoScope S
X-ray source	FOMM 230 01.WTT from Werth
Target/Anode	transmission mode
Filter	Al (1 mm)
Voltage	150 kV
Current	160 μA
Focal spot size	5 μm
Tube to detector	510 mm
Tube to object	185 mm
Detector	TD300V
Definition	1133×1461 pixels (2×2 binning)
Number of projections	800
Angular amplitude	360°
Frame average	20 per projection
Frame rate	333 fps
Acquisition duration	2 h 35 min
Reconstruction algorithm	Filtered back projection
Gray levels amplitude	8 bits
Volume size	540×702×998 voxels (after crop)
Field of view	4.7×6.2×8.7 mm^3 (after crop)
Image scale	8.7 μm/voxel
Pattern	see Fig. 3

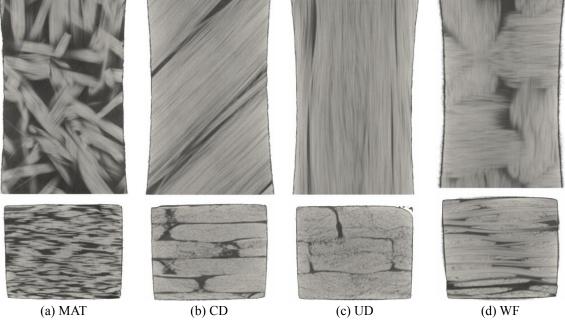(a) MAT   (b) CD   (c) UD   (d) WF

Fig. 3 Front and top mid-slices of the scanned FRPs with four different fiber architectures

in terms of microstructural (i.e., texture) quality for DVC analyses, it is noted that CD, UD and WF architectures resulted in poor contrast since image gradients was low, and thus expected to be more challenging for DVC analyses.

The common way of quantifying the volume fraction of constituents is by thresholding gray level images and following the summation of the remaining voxels that belong to a certain constituent. Thresholding is a very simple segmentation operation that consists in determining the phase of a voxel based on its gray level, and it is particularly adapted for images where only two phases exist. In Table 2, the portion of glass fiber and vinylester matrix are reported depending on the fiber architecture. MAT had the lowest portion of fibers, which in combination with stochastically distributed glass yarns, resulted in the most appropriate texture for correlation analyses. Due to similar yarn orientations, namely, orthogonal yarn distributions, CD and WF had approximately the same portion of fibers (i.e., $\approx$85%). The most challenging microstructure to be analyzed via DVC corresponds to the UD architecture since it had only 8% volume fraction of matrix.

Table 2 Volume fraction of the constituents for the investigated GFRP composites

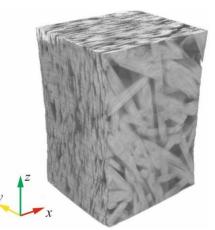| Fiber architecture	Glass fiber, V_{fiber} (%)	Vinylester matrix, V_{matrix} (%)
MAT	71	29
CD	85	15
UD	92	8
WF	88	12

3. 3D full-field measurement technique

In order to measure the 3D kinematics from volumetric images, different strategies have been followed. The most classical one is to work with subset-based DVC (i.e., local approach) where pointwise descriptions of displacement fields are sought. The displacements are measured independently (i.e., locally) and the sole information is that of the subset center. Displacement fields are obtained by subsequent interpolation of these discrete data. The size of the subset corresponds to a natural regularization of the registration.
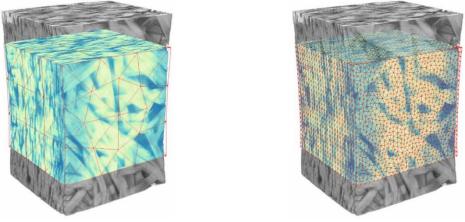
In order to decrease the spatial resolution, some additional hypothesis can be made. The most basic way is to consider the sought displacement field to be continuous. The measured fields are decomposed over any basis that fulfills this constraint. For instance, Roux *et al.* (2008) proposed a finite element (FE) basis. Such FE-based correlation is performed over the entire ROI.

An additional regularization of global DVC, namely, minimizing the equilibrium gap, can significantly decrease the measurement uncertainty and break the unavoidable compromise between measurement error and spatial resolution (Leclerc *et al.* 2012). Moreover, mechanically-based regularization in an FE formulation of DVC was shown to lead to a reduction of uncertainty levels for artificial nonuniform displacement fields (Mendoza *et al.* 2019). The application of the same methodology to a real experimental case showed that even poor image contrast could be dealt with success (Tomičević *et al.* 2013), which is especially important when dealing with natural microstructures.

In this study, global and regularized DVC algorithms was employed to measure 3D displacement fields. In the following, they will be referred as standard FE-DVC and regularized DVC protocols,

(a) Reconstructed 3D scan of the GFRP with MAT fiber architecture

(b) λ=97 voxel   (c) λ=12 voxel

Fig. 4 3D rendering of the MAT architecture (gray level map) and its corresponding ROI (parula color map) considered in DVC analyses. Over the chosen ROI, different discretizations were constructed

respectively. The DVC codes were implemented within the *Correli 3.0* framework (Leclerc *et al.* 2015). Before performing DVC analyses, it was necessary to create 3D meshes consistent with the sample geometry. To match the boundaries of specimens, the 3D image (Fig. 4(a)) was segmented considering the gray levels associated with surrounding air. Afterward, the chosen ROI (Fig. 4(b)-(c)) of the binary image was meshed via the *iso2mesh* algorithm (Tran *et al.* 2020) and exported to an STL file. Finally, the outer surfaces were smoothened and remeshed in *GMSH* (Geuzaine and Remacle 2009). FE meshes with different element lengths (Fig. 4(b)-(c)) were created with first-order tetrahedral elements.

3.1 Global DVC

The main postulate of local and global DVC is based upon the conservation of the gray levels

$$f(\mathbf{x}) = g(\mathbf{x} + \mathbf{u}(\mathbf{x})), \tag{1}$$

where f and g define the gray level (GL) intensities of each voxel, whose position is defined by vector **x,** of an image acquired in referenced and deformed configurations, respectively, and **u** the unknown displacement field. The DVC technique used in this work consisted in minimizing the sum of squared differences Φ_c^2 over the region of interest (ROI)

$$\Phi_c^2 = \int_{\text{ROI}} \varphi_c^2(\mathbf{x}) \mathrm{d}\mathbf{x}, \tag{2}$$

where φ_c defines the map of correlation residuals

$$\varphi_C(\mathbf{x}) = f(\mathbf{x}) - g(\mathbf{x} + \mathbf{u}(\mathbf{x})). \tag{3}$$

Since the minimization problem is ill-posed, the sought displacement field is expressed as

$$\mathbf{u}(\mathbf{x}) = \sum_n u_n \mathbf{\psi}_n(\mathbf{x}) \tag{4}$$

where $\mathbf{\psi}_n$ are the chosen vector fields, and u_n the associated degrees of freedom.

To circumvent the nonlinear aspect of the minimization problem, a Gauss-Newton iterative procedure is followed to obtain the corrections $\{\delta\mathbf{u}\}$ to the measured degrees of freedom from the following linear systems

$$[\mathbf{M}]\{\delta\mathbf{u}\} = \{\mathbf{b}^i\} \tag{5}$$

where $[\mathbf{M}]$ represents the DVC matrix collecting shape functions and the reference image gradient, while $\{\mathbf{b}^i\}$ is the residual vector computed at each iteration i. The convergence of the algorithm is obtained when the L2-norm of $\{\delta\mathbf{u}\}$ becomes less than 10^{-4} voxel.

3.2 Regularized DVC

In order to further decrease the measurement uncertainty of global DVC, additional constraints may be introduced. One path to make the correlation technique more efficient can be performed by assuming locally elasticity and associated equilibrium. The regularization term then acts as a filter that takes into account only mechanically admissible fields. In this work, mechanical admissibility in an FE sense was applied in linear elasticity. The equilibrium equations read

$$[\mathbf{K}]\{\mathbf{u}\} = \{\mathbf{f}\}, \tag{6}$$

where $[\mathbf{K}]$ defines the stiffness matrix, and $\{\mathbf{f}\}$ the column vector collecting the nodal forces. If equilibrium is not satisfied, nodal force residuals

$$\{\mathbf{f}_r\} = [\mathbf{K}]\{\mathbf{u}\} - \{\mathbf{f}\} \tag{7}$$

arise. Hence, the second cost function Φ_c^2, beside the correlation functional, that needs to be minimized becomes

$$\Phi_m^2 = \{\mathbf{u}\}^t [\mathbf{K}_m]^t [\mathbf{K}_m]\{\mathbf{u}\}, \tag{8}$$

where t is the transposition operator, and $[\mathbf{K}_m]$ the rectangular stiffness matrix associated with bulk nodes and Neumann DOFs (i.e., load-free surface nodes). Φ_c^2 corresponds to the sum of the squared norm of all equilibrium gaps at bulk nodes and Neumann DOFs.

Finally, a third cost function is introduced to minimize the traction fluctuations of Dirichlet DOFs

$$\Phi_S^2 = \{\mathbf{u}\}^t [\mathbf{K}_S]^t [\mathbf{L}][\mathbf{K}_S]\{\mathbf{u}\} \tag{9}$$

where $[\mathbf{K}_S]$ corresponds to the partial stiffness matrix for Dirichlet nodes, and $[\mathbf{L}]$ the discrete Laplace-Beltrami operator (Mendoza *et al.* 2019).

Regularized DVC consists in the minimization of the weighted sum of three aforementioned cost functions

$$\Phi_t(\{\mathbf{u}\}) = \widehat{\Phi}_c^2(\{\mathbf{u}\}) + \omega_m \widehat{\Phi}_m^2(\{\mathbf{u}\}) + \omega_S \widehat{\Phi}_s^2(\{\mathbf{u}\}). \tag{10}$$

The correlation, equilibrium gap and loaded surface residuals are normalized with a trial displacement field **v,** in the form of a pure shear wave. The normalized cost functions become

$$\begin{aligned} \widehat{\Phi}_c^2 &= \frac{\Phi_c(\{\mathbf{u}\})}{\{\mathbf{v}\}^t[\mathbf{M}]\{\mathbf{v}\}}, \\ \widehat{\Phi}_m^2 &= \frac{\Phi_m(\{\mathbf{u}\})}{\Phi_m(\{\mathbf{v}\})}, \\ \widehat{\Phi}_s^2 &= \frac{\Phi_s(\{\mathbf{u}\})}{\Phi_m(\{\mathbf{v}\})}, \end{aligned} \tag{11}$$

Furthermore, ω_m and ω_S are weights put on the two penalty terms such that

$$\omega_m = (\ell_m |\boldsymbol{k}|)^4, \omega_S = (\ell_S |\boldsymbol{k}|)^4, \tag{12}$$

where ℓ_m and ℓ_s denote regularization lengths, and $|\mathbf{k}|$ the shear wave number of the trial field. The larger the regularization lengths (expressed in voxels), the more weight is put on the penalty terms, the lower the corresponding cost functions.

4. Protocol of uncertainty quantification

The measurement uncertainty of full-field measurement techniques (e.g., DVC) is evaluated by following different paths. If only one image was acquired at a certain state, usually unloaded, a known displacement field is commonly prescribed in order to generate a deformed volume. The simplest approach of applying artificial motions is to prescribe uniform translations to construct a new volume that is subsequently registered (Roux *et al.* 2008, Benoit *et al.* 2009). Furthermore, displacement fields mimicking localization phenomena may also be prescribed to quantify uncertainties related to discontinuous enrichments (Rannou *et al.* 2010). Such uncertainty analysis probes errors associated with gray level interpolations for achieving sub-voxel resolutions.

The second protocol is also based upon a single 3D scan. However, random noise is added to this reference volume to create a 'deformed' volume (Leclerc *et al.* 2011). The correlation procedure is applied between the noise-free (i.e., reference) and noise-polluted (i.e., deformed) volumes. The aim of such an approach is to study noise sensitivity of DVC. Closed-form solutions were derived and enable for *a priori* predictions of noise influence (Leclerc *et al.* 2012, Hild *et al.* 2016).

The third way of identifying measurement uncertainties is based upon purely acquired data, where the correlation analysis is performed on two consecutively acquired images. The images are usually captured in the unloaded state, with or without any motion applied to the sample (Buljac *et al.* 2018a). The proposed procedure provides the information about the noise level associated with

the CT scanner equipment, acquisition parameters and the applied reconstruction algorithm. Furthermore, rigid body motions may also be deliberately prescribed onto the measuring object between the acquisition of the two subsequently acquired images (Buljac *et al.* 2018c). The main advantage of this protocol is that both sources of error (i.e., actual acquisition noise and interpolation schemes of the correlation algorithm when small motions are applied) are investigated at the same time.

The method applied in this work consisted in analyzing two consecutive scans of samples in the unloaded state (with no rigid body motions being prescribed) since the aim of this study was to determine the measurement uncertainty associated with the fiber architecture of the investigated GFRPs. The acquisition noise level is expected to be approximately the same since unique acquisition parameters were applied to the four GFRPs (Table 1).

5. Displacement and strain uncertainties

In the following, the measurement uncertainties of FE-based and regularized DVC are presented. The analysis was performed between the two subsequently acquired 3D scans with *Correli 3.0*. Nine meshes, with different element lengths (see Table 3), over the same ROI were used to measure displacement fields. The measurement uncertainty was evaluated as the standard deviation of the nodal displacements about its mean value. The change in standard displacement uncertainty with respect to the element length is reported. Regularized DVC was used to estimate the lowest regularization length that satisfied a selected level of standard displacement uncertainty (i.e., $\overline{\sigma}_U=10^{-1}$ voxel). The regularized approach was probed on a single (and fine) mesh with an element length of 12 voxels. The influence of the regularization length was also studied.

The same protocol was followed for standard FE-based and regularized DVC analyses on the four architectures. The mean displacement $\overline{\sigma}_U$ and mean eigen strain $\overline{\sigma}_\varepsilon$ uncertainties will be compared.

Table 3 DVC analysis parameters

	FE-DVC	Regularized DVC
DIC software	*Correli* 3.0 (Leclerc *et al.* 2015)	
Image Filtering	none	
Mean element length (voxels)	97, 76, 56, 42, 30, 23, 16, 12 and 8	12
Shape functions	linear (T4)	
Matching criterion	(penalized) sum of squared differences	
Regularization length (voxels)	none	256, 192, 128, 96, 64, 48, 32, 24, 16
Interpolant	cubic	

5.1 FE-based DVC

Nine independent analyse with different element lengths were conducted. All meshes were discretizing the same ROI. The standard measurement uncertainties for the MAT fiber is shown in Fig. 5. From the measured displacement fields in *x*, *y* and *z* directions, the lowest uncertainty was
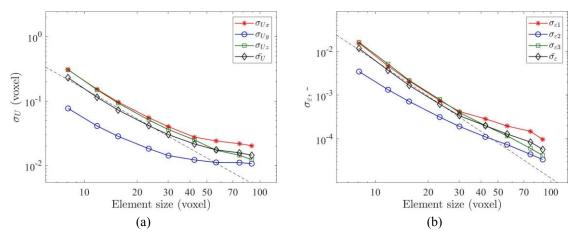
Fig. 5 (a) Displacement and (b) strain uncertainties vs. element size obtained via FE-based DVC applied to the MAT architecture. The black dashed lines denote the power law interpolation and the mean uncertainties

achieved in the *y*-direction, while significantly higher values were observed for element lengths greater than 30 voxels. The longitudinal components (in *x*- and *z*-directions) had approximately the same levels.

From the measured displacement fields, eigen strain fields were computed. The strain uncertainties were calculated as the standard deviation of the nodal strains. The major and minor eigen strains lead to similar levels, while $\sigma_{\varepsilon 2}$ had the lowest strain fluctuations. The change in standard strain uncertainty could be approximated with a power of slope -2.5. Prior to saturation, the standard displacement uncertainty could be interpolated by a power of -1.5, which shows that it is mainly due to Gaussian acquisition noise (Buljac *et al*. 2018a). In order to compare DVC uncertainties with respect to fiber architectures, the root mean square displacement/strain uncertainties $\overline{\sigma}_U$ were also computed.
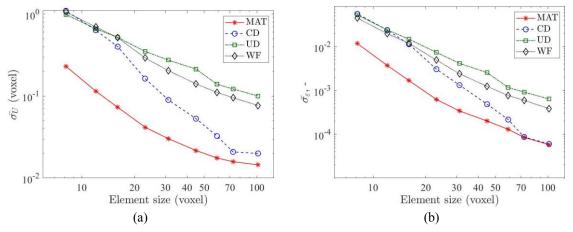

Fig. 6 (a) Mean displacement and (b) strain uncertainties vs. element size for FE-DVC applied to the four architectures

Fig. 6 shows the standard uncertainties of the four investigated GFRPs. The MAT architecture resulted in the lowest displacement and strain uncertainties. For the largest element lengths (97 and 76 voxels), the CD architecture reachee approximately the same uncertainty levels as the MAT GFRP. However, for the element lengths larger than 76 voxels, DVC measurement resolution curve of the CD fiber architecture led to a higher slope. From displacement and strain resolutions, it can be noted that UD and WF fiber architectures report the highest levels of measurement error. Moreover, their microstructural image gradient resulted in one order of magnitude higher uncertainty levels than those obtained from MAT microstructure.

Taking into account the recommended criterion for displacement uncertainty (equal to 10^{-1} voxel), the corresponding element lengths were obtained (Table 4). The MAT GFRP could be analyzed with an element length λ=12 voxels. The corresponding microstructure enabled for the detection of smaller displacement fluctuations (possibly due to damage inception). Conversely, UD and WF architectures requiree the use of meshes with the largest element lengths, namely 96 and 68 voxels, respectively. With FE-based DVC, it would thus be very difficult to measure very fine kinematic fluctuations. Cross-directional fiber orientations provided reliable displacements for elements larger than 30 voxels, while for λ<20 voxels approximately the same uncertainty levels are obtained as with WF and UD architectures.

Table 4 Recommended element length for GFRP composites with different architectures

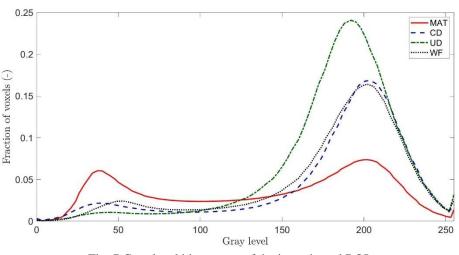| Fiber architecture	Element length, λ (voxel)
MAT	14
CD	30
UD	95
WF	68

Fig. 7 Gray level histograms of the investigated ROIs

In order to understand the change of measurement uncertainty, the gray level histograms (Fig. 7) over the entire ROI are compared. The MAT architecture provided a bimodal histogram, while the

other ones followed left skewed distributions. The lowest measurement uncertainty (MAT architecture) was due to the widest distribution. Conversely, the UD sample partially covered the dynamic range, thereby resulting in the highest uncertainty levels. The proposed study confirms the importance of performing such uncertainty quantification before dealing with mechanically deformed images since contrast and acquisition quality strongly impact the reliability of measured fields.

One additional piece of information that is very useful when comparing different architectures is related to the evaluation of the mean contrast (Leclerc *et al*. 2012, Hild *et al*. 2016). It corresponds to the root mean squared norm of the image gradient over each considered ROI. Table 5 shows that there is a significant difference for the MAT architecture, and to a lesser degree between CD and the other two. This trend is totally consistent with the results reported in Fig. 6 and Table 4.

5.2 Regularized DVC

The following section presents the measurement uncertainties obtained with regularized DVC. First, a comparison between FE-based and regularized DVC is presented for the MAT case (see Fig. 8). For FE-based DVC, the change of measurement uncertainty was reported with respect to the element size. Regularized DVC was conducted on a single mesh with an element length λ=12 voxels, and nine regularization lengths were prescribed to find the minimum one that satisfied the suggested displacement uncertainty level.

Table 5 Mean contrast of the investigated fiber architectures

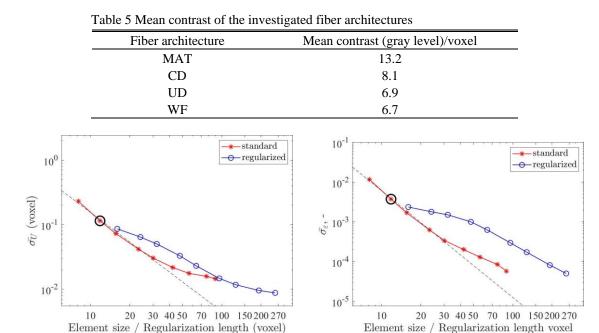| Fiber architecture	Mean contrast (gray level)/voxel
MAT	13.2
CD	8.1
UD	6.9
WF	6.7

(a) (b)

Fig. 8 Comparison between FE-based and regularized DVC analyses applied to the MAT architecture. (a) Displacement and (b) strain uncertainties vs. element/regularization lengths. The black dashed lines denote the power law interpolation for the mean uncertainties of FE-based DVC

When comparing the two DVC approaches, it is noted that regularized DVC outperformed FE-based DVC in terms of displacement and strain uncertainties. The regularized analyses led to lower errors than FE-DVC with an equal element length of 12 voxels. Furthermore, the uncertainty levels obtained with regularization lengths greater than 96 voxels led to lower levels than those of FE-DVC even when the largest element size (λ=97 voxels) was used.

With regularized DVC, the beginning of saturation is observed for regularization lengths less than 32 voxels. From a previous work (Tomičević *et al.* 2013), it was expected that regularization lengths less than the element length would not filter out non-mechanical phenomena (i.e., fluctuations induced by noise). The measurement uncertainty would then be equal to that obtained with (unregularized) FE-DVC. The compromise between the standard strain uncertainty and the regularization length is similar for regularized DVC (Fig. 8). The same trend is observed for mean displacement uncertainty. As a first order estimate, the regularization length plays the same role as the element length when FE-DVC and regularized DVC are compared in terms of measurement uncertainties.

The measurement uncertainties of the investigated FRPs obtained via regularized DVC are shown in Fig. 9. The same trends as for FE-DVC are observed (Fig. 6), namely, the MAT architecture led to the lowest measurement uncertainties for all selected regularization lengths, while UD and WF GFRPs induced the highest measurement errors. However, when large regularization lengths are applied (ℓ_m >128 voxels) all fiber architectures achieved one order of magnitude lower measurement uncertainties than those obtained with FE-DVC for the same element length.
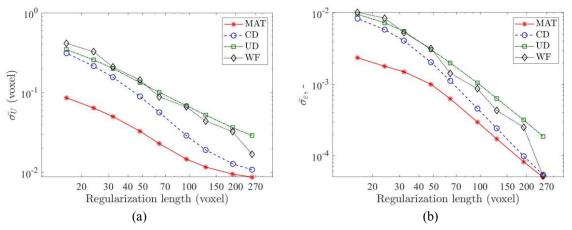

(a)	(b)

Fig. 9 Mean displacement and (b) strain measurement uncertainty for different fiber architecture obtained with regularized DVC approach

Even though very large regularization lengths yielded the lowest measurement uncertainty, their application should be considered with caution. Very large regularization lengths prevent from assessing very small displacement fluctuations (Tomičević *et al.* 2013). If large regularization lengths are selected, they should be used as initial guess when searching for unknown displacement field or the user has to be sure that elasticity is relevant. When small regularization lengths are then reached, they may provide more reliable displacement fields. Therefore, in this investigation the regularization lengths that provide the recommended displacement uncertainty (i.e., $\overline{\sigma}_U = 10^{-1}$ voxel)

are reported in Table 6 for different fiber architectures. The MAT architecture required just slightly larger regularization lengths than the element length. The largest regularization length needed to be applied to UD and WF microstructures, which are almost five times larger than the element length. For FE-DVC, at least 30 voxel element length was needed the for the CD architecture, suggesting a regularization length of 43 voxels when the element length λ=12 voxels.

Table 6 Recommended regularization lengths for GFRP composites with different fiber architecture

Fiber architecture	Regularization length, ℓ_r (voxel)
MAT	16
CD	43
UD	65
WF	59

5. Conclusions

The presented study dealt with the quantification of DVC measurement uncertainties applied to four different fiber architectures. As opposed to DIC, DVC measurements track microstructural features based upon the natural contrast of the observed material. Thus, in order to decrease displacement, and consequently strain uncertainties, FE-DVC was regularized with the equilibrium gap. The regularization procedure applied herein confirmed that the compromise between spatial resolution (i.e., element length) and measurement uncertainty could be partially broken. Such regularization thus enables localized phenomena to be detected and quantified more easily. The most important conclusion drawn from these investigations were:
• The performance of DVC runs strongly depended on microstructural features of GFRP composites (i.e., fiber orientation, yarn misalignment, manufacturing defects).
• The proposed study confirmed the importance of performing uncertainty quantification before dealing with mechanically deformed images since contrast and acquisition quality strongly impacted the reliability of measured fields.
• The mean contrast of the acquired volumetric images was correlated with measurement uncertainties.
• Mechanical regularization coupled with FE-based DVC led to very significant reductions in spurious displacement and strain fluctuations for very fine meshes.

Acknowledgments

References

Agyei, R.F., Hanhan, I. and Sangid, M.D. (2020), "Detecting damage initiation in short fiber composites via

in-situ X-ray tomography and digital volume correlation", *Compos. Commun.*, **22**, 100524. https://doi.org/10.1016/j.coco.2020.100524.

Arif, M.F., Saintier, N., Meraghni, F., Fitoussi, J., Chemisky, Y. and Robert, G. (2014) "Multiscale fatigue damage characterization in short glass fiber reinforced polyamide-66", *Compos. Part B Eng.*, **61**, 55-65. https://doi.org/10.1016/j.compositesb.2014.01.019.

Bay, B.K., Smith, T.S., Fyhrie, D.P. and Saad, M. (1999), "Digital volume correlation: Three-dimensional strain mapping using X-ray tomography", *Exp. Mech.*, **39**, 217-226. https://doi.org/10.1007/BF02323555.

Benoit, A., Guérard, S., Gillet, B., Guillot, G., Hild, F., Mitton, D., Périé, J.N. and Roux, S. (2009), "3D analysis from micro-MRI during in situ compression on cancellous bone", *J. Biomech.*, **42**(14), 2381-2386. https://doi.org/10.1016/j.jbiomech.2009.06.034.

Besnard, G., Hild, F. and Roux, S. (2006), ""Finite-Element" displacement fields analysis from digital images: Application to Portevin-Le Châtelier bands", *Exp. Mech.*, **46**, 789-803. https://doi.org/10.1007/s11340-006-9824-8.

Brynk, T., Molak, R.M., Janiszewska, M. and Pakiela, Z. (2012), "Digital image correlation measurements as a tool of composites deformation description", *Comput. Mater. Sci.*, **64**, 157-161. https://doi.org/10.1016/j.commatsci.2012.04.034.

Buljac, A., Jailin, C., Mendoza, A., Neggers, J., Taillandier-Thomas, T., Bouterf, A., Smaniotto, B., Hild, F. and Roux, S. (2018a), "Digital volume correlation: review of progress and challenges", *Exp. Mech.*, **58**, 661-708. https://doi.org/10.1007/s11340-018-0390-7.

Buljac, A., Trejo Navas, V.M., Shakoor, M., Bouterf, A., Neggers, J., Bernacki, M., Bouchard, P.O., Morgeneyer, T.F. and Hild, F. (2018b), "On the calibration of elastoplastic parameters at the microscale via X-ray microtomography and digital volume correlation for the simulation of ductile damage", *Eur. J. Mech. A Solid.*, **72**, 287-297. https://doi.org/10.1016/j.euromechsol.2018.04.010.

Buljac, A., Taillandier-Thomas, T., Helfen, L., Morgeneyer, T.F. and Hild, F. (2018c), "Evaluation of measurement uncertainties of digital volume correlation applied to laminography data", *J. Strain Anal. Eng. Des.*, **53**(2), 49-65. https://doi.org/10.1177/0309324717748097.

Chambers, A.R., Earl, J.S., Squires, C.A. and Suhot, M.A. (2006), "The effect of voids on the flexural fatigue performance of unidirectional carbon fibre composites developed for wind turbine applications", *Int. J. Fatig.*, **28**(10), 1389-1398. https://doi.org/10.1016/j.ijfatigue.2006.02.033.

Chu, T.C., Ranson, W.F. and Sutton, M.A. (1985), "Applications of digital-image-correlation techniques to experimental mechanics", *Exp. Mech.*, **25**, 232-244. https://doi.org/10.1007/BF02325092.

Croom, B.P., Burden, D., Jin, H., Vonk, N.H., Hoefnagels, J.P.M., Smaniotto, B., Hild, F., Quintana, E., Sun, Q., Nie, X. and Li, X. (2021), "Interlaboratory study of digital volume correlation error due to x-ray computed tomography equipment and scan parameters: An update from the DVC challenge", *Exp. Mech.*, **61**, 395-410. https://doi.org/10.1007/s11340-020-00653-x.

Davis, G.R. and Elliott, J.C. (2006), "Artefacts in X-ray microtomography of materials", *Mater. Sci. Technol.*, **22**(9), 1011-1018. https://doi.org/10.1179/174328406X114117.

Duchene, P., Chaki, S., Ayadi, A. and Krawczak P. (2018), "A review of non-destructive techniques used for mechanical damage assessment in polymer composites", *J. Mater. Sci.*, **53**, 7915-7938. https://doi.org/10.1007/s10853-018-2045-6.

Garcea, S.C., Sinclair, I. and Spearing, S.M. (2015), "In situ synchrotron tomographic evaluation of the effect of toughening strategies on fatigue micromechanisms in carbon fibre reinforced polymers", *Compos. Sci. Technol.*, **109**, 32-39. https://doi.org/10.1016/j.compscitech.2015.01.012.

Garcea, S.C., Wang, Y. and Withers, P.J. (2018), "X-ray computed tomography of polymer composites", *Compos. Sci. Technol.*, **156**, 305-319. https://doi.org/10.1016/j.compscitech.2017.10.023.

Geuzaine, C. and Remacle, J.F. (2009), "Gmsh: a three-dimensional finite element mesh generator with built-in pre- and post-processing facilities", *Int. J. Numer. Meth. Eng.*, **79**(11), 1309-1331. https://doi.org/10.1002/nme.2579.

Gras, R., Leclerc, H., Hild, F., Roux, S. and Schneider, J. (2015), "Identification of a set of macroscopic elastic parameters in a 3D woven composite: Uncertainty analysis and regularization", *Int. J. Solid. Struct.*, **55**, 2-16. https://doi.org/10.1016/j.ijsolstr.2013.12.023.

Hild, F. and Roux, S. (2012), "Comparison of local and global approaches to digital image correlation", *Exp. Mech.*, **52**, 1503-1519. https://doi.org/10.1007/s11340-012-9603-7.

Hild, F., Bouterf, A. and Roux, S. (2015), "Damage measurements via DIC", *Int. J. Fract.*, **191**, 77-105. https://doi.org/10.1007/s10704-015-0004-7.

Hild, F., Bouterf, A., Chamoin, L., Leclerc, H., Mathieu, F., Neggers, J., Pled, F., Tomičević, Z. and Roux, S. (2016), "Toward 4D mechanical correlation", *Adv. Model. Simul. Eng. Sci.*, **3**(17), 1-26. https://doi.org/10.1186/s40323-016-0070-z.

Leclerc, H., Neggers, J., Mathieu, F., Hild, F. and Roux, S. (2015), Correli 3.0, Agence pour la Protection des Programmes, IDDN.FR.001.520008.000.S.P.2015.0.0.0.31500.

Leclerc, H., Périé, J., Hild, F. and Roux, S. (2012), "Digital volume correlation: What are the limits to the spatial resolution?", *Mech. Ind.*, **13**(6), 361-371. https://doi.org/10.1051/meca/2012025.

Leclerc, H., Périé, J.N, Roux, S. and Hild, F. (2011), "Voxel-scale digital volume correlation", *Exp. Mech.*, **51**(4), 479-490. https://doi.org/10.1007/s11340-010-9407-6.

Lecompte, D., Smits, A., Sol, H., Vantomme, J. and Van Hemelrijck, D. (2007), "Mixed numerical-experimental technique for orthotropic parameter identification using biaxial tensile tests on cruciform specimens", *Int. J. Solid. Struct.*, **44**(5), 1643-1656, https://doi.org/10.1016/j.ijsolstr.2006.06.050.

Lee, S., Jo, E. and Ji, W. (2020), "Digital volume correlation technique for characterizing subsurface deformation behavior of a laminated composite", *Compos. Part B Eng.*, **194**, 108052. https://doi.org/10.1016/j.compositesb.2020.108052.

Mahadik, Y., Brown, K.R. and Hallett, S.R. (2010), "Characterization of 3D woven composite internal architecture and effect of compaction", *Compos. Part A Appl. Sci. Manuf.*, **41**(7), 872-880. https://doi.org/10.1016/j.compositesa.2010.02.019.

Mendoza, A., Neggers, J., Hild, F. and Roux, S. (2019), "Complete mechanical regularization applied to digital image and volume correlation", *Comput. Meth. Appl. Mech. Eng.*, **355**, 27-43/ https://doi.org/10.1016/j.cma.2019.06.005.

Périé, J.N., Calloch, S., Cluzel, C. and Hild, F. (2002), "Analysis of a multiaxial test on a C/C composite by using digital image correlation and a damage model", *Exp. Mech.*, **42**, 318-328. https://doi.org/10.1007/BF02410989.

Rannou, J., Limodin, N., Réthoré, J., Gravouil, A., Ludwig, W., Baietto-Dubourg, M.C., Buffière, J.Y., Combescure, A., Hild, F. and Roux, S. (2010), "Three dimensional experimental and numerical multiscale analysis of a fatigue crack", *Comput. Meth. Appl. Mech. Eng.*, **199**(21-22), 1307-1325. https://doi.org/10.1016/j.cma.2009.09.013.

Rashidi, A., Olfatbakhsh, T., Crawford, B. and Milani, A.S. (2020). "A review of current challenges and case study toward optimizing micro-computed X-Ray tomography of carbon fabric composites", *Mater.*, **13**(16), 3606. https://doi.org/10.3390/ma13163606.

Ray, B.C., Hasan, S.T. and Clegg, D.W. (2007), "Evaluation of defects in FRP composites by NDT techniques", *J. Reinf. Plast. Compos.*, **26**(12), 1187-1192. https://doi.org/10.1177/0731684407079348.

Rolland, H., Saintier, N. and Robert, G. (2016), "Damage mechanisms in short glass fibre reinforced thermoplastic during in situ microtomography tensile tests", *Compos. Part B Eng.*, **90**, 365-377. https://doi.org/10.1016/j.compositesb.2015.12.021.

Roux, S., Hild, F., Viot, P. and Bernard, D. (2008), "Three-dimensional image correlation from X-ray computed tomography of solid foam", *Compos. Part A Appl. Sci. Manuf.*, **39**, 1253-1265. https://doi.org/10.1016/j.compositesa.2007.11.011.

Schöberl, E., Breite, C., Melnikov, A., Swolfs, Y., Mavrogordato, M.N., Sinclair, I. and Spearing, S.M. (2020), "Fibre-direction strain measurement in a composite ply under quasi-static tensile loading using Digital Volume Correlation and in situ Synchrotron Radiation Computed Tomography", *Compos. Part A Appl. Sci. Manuf.*, **137**, 105935. https://doi.org/10.1016/j.compositesa.2020.105935.

Scott, A.E., Mavrogordato, M., Wright, P., Sinclair, I. and Spearing, S.M. (2011), "In situ fibre fracture measurement in carbon-epoxy laminates using high resolution computed tomography", *Compos. Sci. Technol.*, **71**(12), 1471-1477. https://doi.org/10.1016/j.compscitech.2011.06.004.

Tekieli, M., Santis, S.D., Felice, G.D., Kwiecień, A. and Roscini, F. (2017), "Application of Digital Image

Correlation to composite reinforcements testing", *Compos. Struct.*, **160**, 670-688. https://doi.org/10.1016/j.compstruct.2016.10.096.

Tomičević, Z., Hild, F. and Roux, S. (2013), "Mechanics-aided digital image correlation", *J. Strain Anal. Eng. Des.*, **48**(5), 330-343. https://doi.org/10.1177/0309324713482457.

Tran, A.P., Yan, S. and Fang, Q. (2020), "Improving model-based functional near-infrared spectroscopy analysis using mesh-based anatomical and light-transport models", *Neurophotonic.*, **7**(1), 015008. https://doi.org/10.1117/1.NPh.7.1.015008.

Vrgoč, A., Tomičević, Z., Smaniotto, B. and Hild, F. (2021a), "Application of different imaging techniques for the characterization of damage in fiber reinforced polymer", *Compos. Part A Appl. Sci. Manuf.*, **150**, 106576. https://doi.org/10.1016/j.compositesa.2021.106576.

Vrgoč, A., Tomičević, Z., Zaplatić, A. and Hild, F. (2021b), "Damage analysis in glass fibre reinforced epoxy resin via digital image correlation", *Trans. Famena*, **45**(2), 1-12. https://doi.org/10.21278/TOF.452024020.

Wang, B., Zhong, S., Lee, T.L., Fancey, K.S. and Mi, J. (2020), "Non-destructive testing and evaluation of composite materials/structures: A state-of-the-art review", *Adv. Mech. Eng.*, **12**(4), 1-28. https://doi.org/10.1177/1687814020913761.